



A Two-Dimensional Network Simulator for Two-Phase Flow in Porous Media

EYVIND AKER^{1,2}, KNUT JØRGEN MÅLØY¹, ALEX HANSEN^{2,3} and G. GEORGE BATROUNI⁴

¹*Department of Physics, University of Oslo, N-0316 Oslo, Norway*

²*Department of Physics, Norwegian University of Science and Technology, N-7034 Trondheim, Norway*

³*IKU Petroleum Research, N-7034 Trondheim, Norway*

⁴*Institut Non-Linéaire de Nice, Université de Nice - Sophia Antipolis, 06560 Valbonne, France*

(Received: 26 May 1997; in final form: 23 March 1998)

Abstract. We investigate a two-dimensional network simulator that model the dynamics of drainage dominated flow where film flow can be neglected. We present a new method for simulating the temporal evolution of the pressure due to capillary and viscous forces in the displacement process. To model the dynamics, we let the local capillary pressure change as if the menisci move in and out of hour-glass shaped tubes. Furthermore, a method has been developed to allow simultaneous flow of two liquids into one tube. The model is suitable to simulate different time dependencies in two-phase drainage displacements. In this paper, we simulate the temporal evolution of the fluid pressures and analyze the time dependence of the front between the two liquids. The front width was found to be consistent with a scaling relation $w \propto t^\beta h(t/t_s)$. The dynamical exponent, β , describing the front width evolution as function of time, was estimated to $\beta = 1.0$. The results are compared to experimental data of Frette and co-workers.

Key words: network modeling, immiscible, drainage displacement, two-phase flow, capillary and viscous forces, pressure simulations, scaling exponents, front width, time dependences.

1. Introduction

Two-phase displacements in porous media have been intensely studied over the last two decades. The main reason for this is the great variety of structures observed when changing the physical parameters of the fluids such as viscosity contrast, wettability, interfacial tension and displacement rate. Besides being a process of great interest in modern physics, it has a large number of practical applications in many fields of science such as oil recovery and hydrology. Here we concentrate on drainage displacements, i.e. the process where a non-wetting fluid displaces a wetting fluid in porous media.

The main purpose of this paper is to present a network simulator modeling immiscible two-phase flow on a two-dimensional lattice of tubes. With respect to the capillary pressure of menisci the tubes are hour-glass shaped. That is, we take into account the local capillary increase when menisci move into narrower parts of

the tubes. This makes the model closer to the dynamics of drainage dominated flow where film flow can be neglected. Furthermore, we present a new method to simulate the temporal evolution of the global capillary pressure when the viscous pressure gradient is also included.

In slow drainage, the invading fluid is found to suddenly invade a larger region causing another part to retire (bursts) (Haines, 1930; Lenormand and Zarcone, 1983; Måløy *et al.*, 1992). Experiments performed by Måløy *et al.* (1992) have also produced evidence that the bursts are characterized by large pressure fluctuations (Haines jumps). The simulation model describes the burst dynamic successfully due to the capillary variation of menisci that are free to move in both directions inside the tubes. In displacement at higher injection rates where both liquids are found to flow simultaneously into a single tube (Lenormand and Zarcone, 1983; Dullien, 1992) an approximation has been developed to model mixing of the fluids. Additional mechanisms observed in imbibition are not taken into account (Lenormand and Zarcone, 1983; Cieplak and Robbins, 1988).

The different structures in drainage displacements divide into three major flow regimes: viscous fingering (Chen and Wilkinson, 1985; Måløy *et al.*, 1985), stable displacement (Lenormand *et al.*, 1988) and capillary fingering (Lenormand and Zarcone, 1985). There exist statistical models such as DLA (Witten and Sander, 1981), anti-DLA (Paterson, 1984) and invasion percolation (Wilkinson and Willemsen, 1983) that reproduce the basic domains in viscous fingering, stable displacement and capillary fingering, respectively. However, these models do not contain any physical time for the front evolution and they cannot describe the crossover between the major flow regimes.

To investigate the physics of the displacement processes, many network models have been developed over the last two decades (Chen and Wilkinson, 1985; Koplik and Lasseter, 1985; Dias and Payatakes, 1986; King, 1987; Lenormand *et al.*, 1988; Blunt and King, 1990; Constantinides and Payatakes, 1996; Pereira *et al.*, 1996; van der Marck *et al.*, 1997). The models have been used to obtain new information in the different flow regimes and to study statistical properties of the displacement structure. Some others, have been used to calculate macroscopic parameters such as fluid saturations and relative permeabilities. However, most models neglect the local variation in capillary pressure as the invading fluid moves into wider or narrower parts of the channels in contrast to the one we present here.

We have performed three simulations one in each of the regimes: viscous finger, stable displacement and capillary fingering. The resulting pattern formations and pressure evolutions are qualitatively discussed and compared to well known experimental properties of drainage displacement. Furthermore, we have done 17 simulations of displacements with viscosity matching fluids from low to high injection rates. For every simulation the temporal evolution of the front has been analyzed according to the experimental work done by Frette *et al.* (1997). We find that the front width w obey the scaling relation $w \propto t^\beta h(t/t_s)$ with dynamical exponent $\beta = 1.0$. The saturated front width w_s and the saturation time t_s is found to depend on the

capillary number C_a . By fitting the dependencies to power laws of type $w_s \propto C_a^{-\alpha}$ and $t_s \propto C_a^{-\gamma}$ we estimate $\alpha = 0.2$ and $\gamma = 1.1$. The front itself is found to have fractal dimension $D_b = 1.3$, consistent with corresponding experiments performed by Frette *et al.* (1997).

The paper is organized as follows. Section 2 describes the porous medium model and Section 3 addresses the method we used to solve the fluid flow in the network. In Section 4, we present the algorithm updating the menisci before we discuss in Section 5 how the menisci are moved into neighboring tubes. Finally, Section 6 gives the simulation results and in Section 7 some conclusions are drawn.

2. The Porous Medium Model

2.1. GEOMETRY OF MODEL POROUS MEDIUM

The porous medium is represented by a square lattice of tubes inclined at 45° . Thus, if all tubes are equal and a uniform pressure across the lattice is applied, a liquid flows equally well in tubes inclined to the left as tubes inclined to the right. The tubes are connected together at nodes, where four tubes meet. There is no volume assigned to the nodes: the tubes represent the volume of both pores and throats. The liquids flow from the bottom to the top of the lattice and periodic boundary conditions are applied horizontally. The pressure difference between the first (bottom of system) and the last (top) rows defines the pressure across the lattice. Gravity effects are neglected, and as a consequence we consider a horizontal flow in a two-dimensional network of tubes. See Figure 1 for details.

The tubes are cylindrical with equal length d , and every tube is assigned a radius r which is chosen at random in the interval $[\lambda_1, \lambda_2]d$. The randomness of the radii represent the disorder of an ordinary porous medium and λ_1 and λ_2 define the width of the distribution of radii.

2.2. FLUID FLOW THROUGH THE NETWORK

Initially, the system is filled with a defending fluid with viscosity μ_1 . The invading fluid with viscosity μ_2 is injected from the bottom row with a constant injection

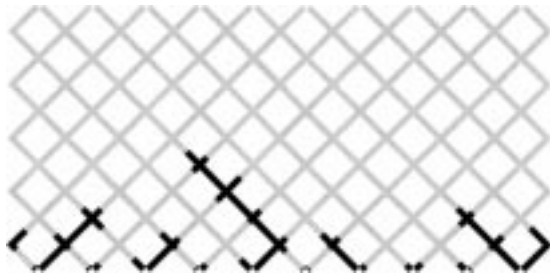


Figure 1. A square lattice of tubes connected together at nodes. The size of the lattice is 10×10 nodes. The black region indicates the invading non-wetting fluid coming from below and the light gray indicates the defending wetting fluid flowing out of the top.

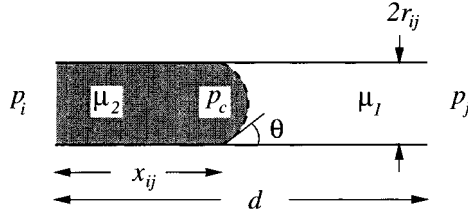


Figure 2. Flow in a tube containing a meniscus.

rate. Here we report on the study of drainage displacements, and so let the invading fluid be non-wetting and the defending fluid be wetting. We assume that the fluids are immiscible and that there is a well defined interface between the two phases. Furthermore, we will treat the liquids as incompressible.

Consider a tube containing both liquids between node i and j in the network as shown in Figure 2. The capillary pressure p_c due to the interface between the two phases (a meniscus) is given by Young–Laplace law

$$p_c = \frac{2\gamma}{r} \cos \theta, \quad (1)$$

where θ refer to the wetting angle between the nonwetting and wetting phases and r is the radius of the tube. γ denotes the interfacial tension between the two phases. In drainage displacement, θ is in the interval $(0, \pi/2)$.

With respect to the capillary pressure we assume that the tubes are hour-glass shaped with effective radii following a smooth function. As a result the capillary pressure of a meniscus will depend on its position inside the tube. We take this effect into account by modifying the Young–Laplace law to obtain

$$p_c = \frac{2\gamma}{r} [1 - \cos(2\pi x)]. \quad (2)$$

Here x is the position of the meniscus in the tube ($0 \leq x \leq 1$) and $\theta = 0$ (perfect wetting). Equation (2) is plotted as a function of x in Figure 3. From Figure 3 we

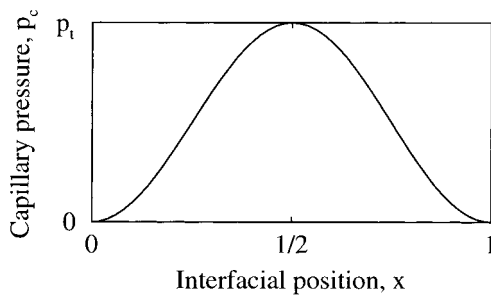


Figure 3. The capillary pressure p_c as a function of the meniscus' position x in that tube. In the middle of the tube at $x = 1/2$ the capillary pressure becomes equal to the threshold pressure p_t .

notice that $p_c = 0$ at the ends of the tube whereas it is equal to the threshold pressure p_t when the meniscus is in the middle of the tube, i.e. $p_t = 4\gamma/r$. The threshold pressure is the minimum pressure required to let the non-wetting fluid invade the tube.

The suggested dependency in p_c (Equation (2)) makes the model closer to the burst dynamics of drainage dominated displacement where film flow can be neglected. A burst is characterized by abruptly fluid invasion. When non-wetting fluid is pumped into the network the menisci moves into narrower parts of the tubes and the capillary pressure increases. Eventually, one meniscus gets unstable and the invading fluid covers new tubes in a burst, accompanied by a retreat of the nearby menisci and a subsequent decrease in capillary pressure (Måløy *et al.*, 1992).

The volume flux q_{ij} through the tube from the i th to the j th node is found from the Washburn equation for capillary flow (Washburn, 1921). As an approximation we treat the tubes as if they were cylindrical and obtain

$$q_{ij} = -\frac{\pi r_{ij}^2 k_{ij}}{\mu_{\text{eff}}} \cdot \frac{1}{d} (\Delta p_{ij} - \tilde{p}_c). \quad (3)$$

Here $k_{ij} = r_{ij}^2/8$ is the permeability, r_{ij} is the average radius of the tubes and $\Delta p_{ij} = p_j - p_i$ is the pressure difference between the i th and the j th node. μ_{eff} and \tilde{p}_c denote the effective viscosity and the total capillary pressure, respectively. They will be defined below.

A tube partially filled with both of the liquids is allowed to contain either one or two menisci leading to four different arrangements as shown in Figure 4. We note that the menisci can have any position between the ends (0 and 1) of the tubes and that they are free to move in both directions. The effective viscosity μ_{eff} , is a sum of the amount of each fluid multiplied by their respective viscosities. The total capillary pressure \tilde{p}_c , is the the sum of the capillary pressures of the menisci that are inside the tube. The absolute value of the capillary pressure of each meniscus is given by Equation (2), while its sign depends on whether the meniscus points upwards such as in Figure 4(a) or downwards such as in Figure 4(b). In the simple case when the tube only contains one meniscus pointing upwards (Figure 4(a)) $\mu_{\text{eff}} = \mu_2 x_{ij} + \mu_1 (1 - x_{ij})$ and $\tilde{p}_c = p_c$. For a tube without menisci $\tilde{p}_c = 0$, and Equation (3) reduces to that describing Hagen–Poiseuille flow with $\mu_{\text{eff}} = \mu_1$ or μ_2 .

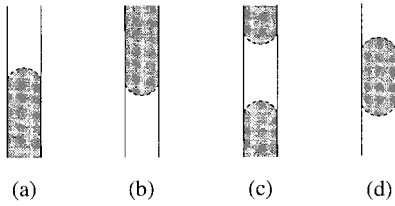


Figure 4. Four different fluid arrangements inside one tube. The shaded and the white regions indicate the non-wetting and wetting fluid respectively.

3. Solving the Flow Field

The fluids are assumed incompressible leading to conservation of volume flux at each node:

$$\sum_j q_{ij} = 0. \quad (4)$$

Here q_{ij} denotes the flow through a tube connecting node i and j . Equation (4) is simply Kirchhoff's equation and in the summation j runs over the nearest neighbor nodes to the i th node. The index i runs over all nodes that do not belong to the top or bottom rows, that is, the internal nodes. This set of linear equations are to be solved with the constraint that the pressures at the nodes belonging to the upper and lower rows are kept fixed.

By inserting Equation (3) in Equation (4) we get:

$$\sum_j g_{ij}(p_j - p_i - p_c) = 0, \quad (5)$$

where g_{ij} defines the mobility of the tube, i.e. $g_{ij} \equiv \pi r_{ij}^2 k_{ij} / \mu_{\text{eff}}$. In order to write this set of equations as a matrix equation, we move all the capillary pressures and the fixed pressure referring to the nodes belonging to the upper and lower rows to the right-hand side of Equation (5). The final matrix equation may then be written as

$$\sum_j D_{ij} p_j = B_i, \quad (6)$$

where the indices i and j only run over internal nodes. D_{ij} are elements a conductance matrix D (Batrouni and Hansen, 1988) where the elements depend on the connection between different tubes and their respective mobility. p_j are the elements in the pressure vector, containing the pressure at the internal nodes and B_i contains the pressure at the boundaries (upper and lower rows) and the capillary pressure if a meniscus is present in the tube.

We are seeking the solution of the pressure at the internal nodes for a given configuration of the menisci, i.e

$$p_j = \sum_i (D^{-1})_{ij} B_i. \quad (7)$$

This equation is solved by using the Conjugate Gradient method (Batrouni and Hansen, 1988).

3.1. SOLVING FOR A CONSTANT INJECTION RATE

For two-phase displacement in a porous medium the injection rate Q is given by

$$Q = A \Delta P + B. \quad (8)$$

Here ΔP is the pressure across the system and A and B are parameters depending on the geometry of the medium and the current configuration of the liquids. The first part of Equation (8) is simply Darcy's law for one phase flow through a porous medium. The last part B results from the capillary pressure between the two phases. As long as the menisci are kept at fixed positions B becomes a constant. To define the global capillary pressure we rewrite Equation (8) into the form

$$\Delta P = \frac{Q}{A} - \frac{B}{A}. \quad (9)$$

The last part $-B/A$ is defined as the global capillary pressure.

The nodal pressures solved by Equation (7) correspond to keeping the applied pressure difference across the network constant. We want to study the temporal evolution of the pressure ΔP and the global capillary pressure $-B/A$ in Equation (9) at constant injection rate Q . To do so we proceed as follow.

The parameters A and B are calculated by solving the nodal pressures (7) for two different pressure $\Delta P'$ and $\Delta P''$ applied across the lattice. The corresponding injection rates Q' and Q'' are calculated. By inserting the pressures and the injection rates into Equation (8) we obtain a set of two equations from which A and B are found

$$Q' = A\Delta P' + B, \quad (10)$$

$$Q'' = A\Delta P'' + B. \quad (11)$$

The next step is to calculate ΔP and relate the nodal pressures to the desired injection rate Q . From Equation (9) we find the pressure ΔP for a given Q when A and B are known. Thus, we could proceed to find the nodal pressures by solving Kirchhoff's equation with this pressure applied on the inlet. That would give the correct flow rates in each tube for the desired Q . However, the following method will save a third solution of Equation (7).

All the equations involved in the calculations have the functional form $f(x) = ax + b$. As a consequence, the pressure Δp_{ij} between node i and j in the lattice becomes a linear function of the pressure ΔP across the system:

$$\Delta p_{ij} = \Gamma_{ij} \Delta P + \Pi_{ij}. \quad (12)$$

Here is Γ_{ij} a dimensionless quantity depending on the mobilities g_{ij} of the tubes and Π_{ij} is a function of the capillary pressures of the menisci inside the tubes. If no menisci are present Π_{ij} is zero. Equation (12) can easily be deduced for two cylindrical tubes with different radii connected in series.

From Equation (3) we can write the flow rate q_{ij} from node i to node j as

$$q_{ij} = a_{ij} \Delta p_{ij} + b_{ij}, \quad (13)$$

where a_{ij} and b_{ij} are parameters depending on the permeability of the tube, the effective viscosity and the capillary pressure due to a meniscus. By inserting Equation (12)

into Equation (13) and redefine a_{ij} 's and b_{ij} 's we obtain a relation between ΔP and q_{ij}

$$q_{ij} = \tilde{a}_{ij} \Delta P + \tilde{b}_{ij}. \quad (14)$$

The parameters \tilde{a}_{ij} and \tilde{b}_{ij} are found from the set

$$q'_{ij} = \tilde{a}_{ij} \Delta P' + \tilde{b}_{ij}, \quad (15)$$

$$q''_{ij} = \tilde{a}_{ij} \Delta P'' + \tilde{b}_{ij}. \quad (16)$$

Here q'_{ij} and q''_{ij} are the flow rates in the tubes that were found for the pressures $\Delta P'$ and $\Delta P''$, respectively. Note that the parameters A and B in (8) and \tilde{a}_{ij} and \tilde{b}_{ij} in (14) all depend on the current position of the menisci and we therefore need to solve them for every new fluid configuration.

The solution due to a constant injection rate can now be summarized into two steps:

1. After we have found A and B from Equations (10)–(11) we use Equation (9) to get ΔP for the desired Q .
2. This ΔP is then used in Equation (14) to get the local flow q_{ij} .

The validity of Equation (12) is easily checked by solving Kirchhoff's equation for the calculated pressure ΔP and compare the solution with the one given from Equation (14). Numerical results show excellent agreement between these two solutions.

4. Updating the Menisci

A time step Δt is chosen such that every meniscus is allowed to travel at most a maximum step length Δx_{\max} during that time step. This leads to the formula

$$\Delta t = \min_{ij} \left[\frac{\Delta x_{\max}}{v_{ij}} \right], \quad (17)$$

where $v_{ij} = q_{ij}/\pi r_{ij}^2$ denotes the flow velocity in a tube containing a meniscus between the i th and the j th node. We note that the time step becomes dependent on the local velocity.

In each time step we check whether or not a meniscus crosses a node. If this happens, the time step is redefined such that this meniscus stops at the end of the tube. A meniscus reaching the end of a tube is moved into the neighbor tubes (see Section 5).

The new positions of the menisci are calculated by using a second order Runge-Kutta scheme (Press *et al.*, 1992). Numerical analysis we have performed show that this scheme produces more stable solutions than the less accurate and more unstable Euler scheme. We use the simulated pressure ΔP across the lattice to establish the stability and convergence properties of the numerical solution (see for example

Figure 9). For the simulations it was verified that the pressure as function of time converges towards a unique solution when $\Delta x_{\max} \leq 0.1d$. That means Kirchhoff's equation must be solved approximately 10–20 times to let a meniscus pass through a single tube. This is probably what we can expect when we want to measure the fluctuations in the pressure due to local capillary changes inside the tubes. With larger step lengths the variations in the capillary pressure are lost and the solution is no longer suitable for our measurements.

When the time step is defined as in Equation (17) the implementation of the second order Runge–Kutta scheme is not straight forward. Before discussing our modifications, we first remind the reader of the Runge–Kutta scheme. Let x_n denote the position of a meniscus at time t_n and let the next position at time $t_{n+1} = t_n + \Delta t$ be x_{n+1} where Δt is the time step found from (17). The second order Runge–Kutta scheme then becomes (Press *et al.*, 1992)

$$x_{n+1} = x_n + k_2 + O(\Delta t^3), \quad (18)$$

$$k_1 = \Delta t \cdot v(t_n, x_n), \quad (19)$$

$$k_2 = \Delta t \cdot v(t_n + \frac{1}{2}\Delta t, x_n + \frac{1}{2}k_1), \quad (20)$$

where $v(t_n, x_n)$ denotes the local flow rate in each tube and $v(t_n + \frac{1}{2}\Delta t, x_n + \frac{1}{2}k_1) \equiv v_{\text{mid}}(t_n, x_n)$ defines the midpoint velocity.

Note that the velocities defining the time step in Equation (17) correspond to the derivative of the curve x_n at the starting point of each time interval, i.e. $v(t_n, x_n) = v_{ij}$, where the subscript ij is omitted on the left-hand side of the equality. When the menisci are updated by using the velocities $v(t_n, x_n)$, Equation (17) leads to the condition

$$|x_{n+1} - x_n| \leq \Delta x_{\max}, \quad (21)$$

for all the menisci. In the second order Runge–Kutta scheme, the next position x_{n+1} is found by using the midpoint velocity $v_{\text{mid}}(t_n, x_n)$, which in general differs from $v(t_n, x_n)$. As a consequence, condition (21) may no longer be valid and the displacement length or the stability of the numerical solution, are no longer controlled. Assume that the position of the menisci is a smooth function of time, the effect vanishes since $v_{\text{mid}}(t_n, x_n) \simeq v(t_n, x_n)$. Moreover, there is no problem as long as $v_{\text{mid}}(t_n, x_n) \leq v(t_n, x_n)$. The problem arises when $v_{\text{mid}}(t_n, x_n) \gg v(t_n, x_n)$ and the final displacement becomes much larger than Δx_{\max} . To avoid this scenario the time step is redefined by inserting the midpoint velocities in Equation (17). A new midpoint velocity corresponding to the redefined time step is calculated and the positions are updated according to this time step by using the new midpoint velocity. The procedure is repeated until the displacements become close enough to the maximum step length Δx_{\max} . Typically, the final displacement must be less than about $1.1 \Delta x_{\max}$. Otherwise, the numerical solution may diverge. After the menisci

are updated, the total time lapse is recorded before the nodal pressures are solved for the new fluid configuration.

5. Motion of the Menisci at the Nodes

When a meniscus reaches the end of a tube it is moved into the neighbor tubes according to some defined rules. These rules take care of the different fluid arrangements that can appear around the node. Basically, the non-wetting fluid can either invade into or retreat from the neighbor tubes as shown in Figure 5(a) and (b), respectively. In 5(a) the non-wetting fluid approaches the node from below (drainage). When the meniscus has reached the end of the tube (position 1), it is removed and three new menisci are created at position δ in the neighbor tubes (position 2). The distance δ is about 1–5% of the tube length d and it defines the node region where the capillary pressure is zero. The node region avoids that the created menisci at position 2 immediately disappear and move back to the initial position 1 in tubes where the flow direction is opposite to the direction of the invading fluid. The node region has also an important role that allows mixing of the liquids (see below).

Figure 5 (b) shows the opposite case when the non-wetting fluid retreats into a single tube (imbibition). As Figure 5 shows the properties of imbibition should not be neglected as long as the menisci can travel in both directions. However, in drainage which is what we are focusing on, arrangement (b) will appear rarely compared to (a).

When the menisci are moved a distance δ into the neighbor tubes the total time lapse is adjusted due to the injection rate of the invading fluid. The adjustment is calibrated such that the amount of the invading fluid in the lattice always equals the injected volume. The injected volume is the product of the time lapse and the injection rate.

Difficulties arise when we want to create a new meniscus in a tube that already contains two menisci. To allow such movement the two original menisci and the new meniscus are merged into one by the following method. Consider a scenario as in

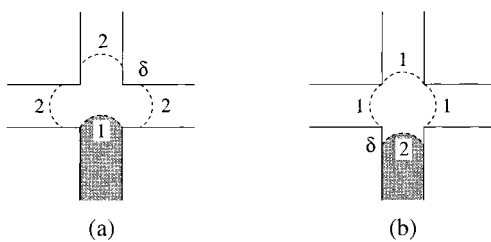


Figure 5. The motion of the menisci at the nodes. (a): The non-wetting fluid (shaded) reaches the end of the tube (position 1) and is moved a distance δ into the neighbor tubes (position 2). (b): The wetting fluid (white) reaches the end of the tubes (position 1) and the non-wetting fluid (shaded) retreat to position 2. For both (a) and (b) a proper time is recorded due to the small movement δ .

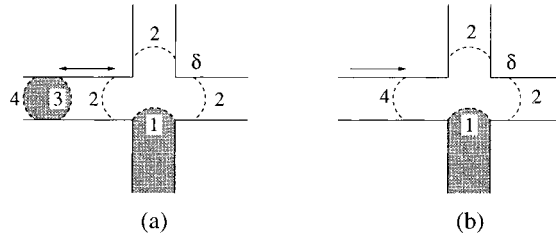


Figure 6. Reduction of three menisci into one. (a) The non-wetting fluid has reached the end of the tube (position 1) and is going to be moved into the neighbor tubes (position 2). The three menisci in the left tube are reorganized causing the situation shown in (b) to appear. In the figures the arrows denote the length of the wetting fluid between position 2 and 3 which is equal to the distance the meniscus at position 4 is moved to the right.

Figure 5(a) but assume now that the leftmost tube already contains a bubble of non-wetting fluid as shown in Figure 6(a). To merge the three menisci in the leftmost tube into one, we move the wetting fluid between positions 2 and 3 to the left side of the non-wetting bubble and remove the menisci at positions 2 and 3 before the meniscus at position 4 is moved to the right a distance equal to the original length between positions 2 and 3 (Figure 6(b)). The same principles apply when the non-wetting fluid retreat into a tube that already contains a bubble of wetting fluid.

5.1. MIXING OF THE FLUIDS

The moving rules described in Figures 5 and 6 solve the problem of modeling a 'mixture' of the two liquids. Consider the situations shown in Figure 7 where both the non-wetting and wetting fluids flow toward the node from the bottom and right tube respectively. Physically, it is expected that the fluid flowing out of the node is a mixture of both liquids. It is observed (Lenormand and Zarcone, 1983; Dullien, 1992) that such simultaneous flow of both liquids in a tube takes place in so-called funicular continuous flow or a discontinuous dispersed flow. In the former case the wetting phase flows along the cylinder wall surrounding the non-wetting phase, which occupies the central portion of the tube. A discontinuous flow is characterized by a dispersed non-wetting phase flowing as isolated droplets in a continuous wetting phase.

A model describing funicular and dispersed flow would be too complicated. Instead, we assume that the simultaneous flow can be represented by a finite number of small bubbles of each liquid, placed next to each other inside the tube. By sorting the bubbles of same type of fluid they can be replaced by one or two menisci. The procedure is illustrated with an example in Figure 7. When the meniscus in the bottom tube reaches the end of the tube it is moved a distance δ into the neighbor tubes (arrangements a and b). Due to the opposite flow direction in the right tube the created meniscus in this tube flows back to the node (arrangement c) and is moved into the neighbor tubes (arrangement d). Now, the new meniscus in the bottom tube

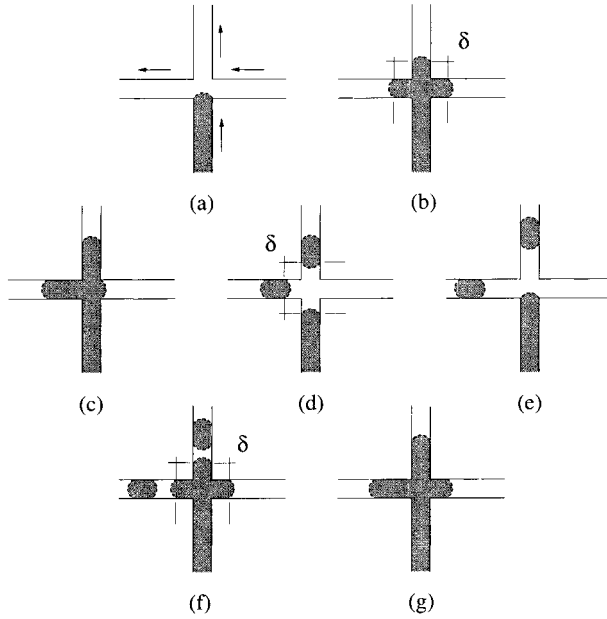


Figure 7. A 'mixture' of non-wetting (shaded) and wetting (white) which flow into the neighbor tubes. The different arrangements (a)–(g) are a result of applying the rules which are described earlier in this section. For all figures the fluids flow towards the node from the bottom and right tube while the fluids in the top and the left tube flow away from it (denoted by the arrows in (a)).

again approaches the node from below (arrangement e) and creates a configuration with three menisci in the top and left tubes (arrangement f). To avoid the number of menisci inside a single tube to become greater than two, the three menisci at the top and the left tube are reduced to one by placing the wetting fluid on the top of the non-wetting one (arrangement g).

The reorganization when three menisci are reduced to one (Figures 6 and 7) results in unphysical jumps in the capillary pressure. Due to the small size of the bubbles, the jumps usually appear as perturbations in the total pressure. A small number of such jumps will not affect the numerical solution very much. But, the moment they become more dominant the numerical solution gets unstable and diverges.

6. Simulations

In two-phase fluid displacement there are mainly three types of forces: viscous forces in the invading fluid, viscous forces in the defending fluid and capillary forces due to the interface between them. This leads to two dimensionless numbers that can characterize the flow in porous media: the capillary number C_a and the viscosity ratio M .

The capillary number is a quantity describing the competition between capillary and viscous forces. It is defined as

$$C_a = \frac{Q\mu}{\Sigma\gamma}, \quad (22)$$

where Q (cm²/s) denotes the injection rate, μ (Poise) is the maximum viscosity of the two fluids, Σ (cm²) is the cross section of the inlet and γ (dyn/cm) is the interfacial tension between the two phases. Σ is the product of the length of the inlet and the mean thickness of the lattice due to the average radius of the tubes.

M defines the ratio of the viscosities of the two fluids and is given by the invading viscosity μ_2 divided with the defending viscosity μ_1 :

$$M = \frac{\mu_2}{\mu_1}.$$

We have performed three simulations where we discuss qualitatively the behavior of the global capillary pressure as well as the pressure across the lattice. There is one simulation in each of the regimes of interest: viscous fingering, stable displacement and capillary fingering. Furthermore, we have run 17 simulations with viscosity matching fluids ($M = 1.0$) at different injection rates. In this set we have analyzed the dependency of the front geometry on the capillary number and compared our data with experimental result from Free *et al.* (1997).

All simulations were performed with parameters as close as possible to experiments done by Måløy *et al.* (1985) and Frette *et al.* (1997). The length d of all tubes in the lattices were set equal to 1 mm and the radii r of the tubes were chosen randomly in the interval $0.05d \leq r \leq d$. The interfacial tension was set to $\gamma = 30$ dyn/cm and the viscosities of the defending and the invading fluids varied between 0.01 P (\simeq water) and 10 P (\simeq glycerol). The simulations were ran on a Cray T90 vector machine.

6.1. VISCOUS FINGERING

Figure 8 shows the result of a simulation in the regime of viscous fingering performed on a lattice of 60×80 nodes. The corresponding pressure across the lattice (a) and the global capillary pressure (b) as functions of time are shown in Figure 9. The injection rate was $Q = 1.5$ ml/min and the fluid viscosities were $\mu_2 = 0.010$ P $<$ $\mu_1 = 10$ P giving $C_a = 4.6 \times 10^{-3}$ and $M = 1.0 \times 10^{-3}$.

The pattern formation (Figure 8) shows that the invading fluid creates typical fingers into the defending fluid. The fingers are driven by viscous forces in the defending fluid and the capillary forces of the menisci are less dominant.

Due to the constant injection rate the pressure across the lattice (Figure 9(a)) decreases as the less viscous fluid invades the system. The rate of which it decreases is non-trivial and is expected to depend on the fractal development of the fingers. The rapid decrease at the end of the pressure function corresponds to the breakthrough of

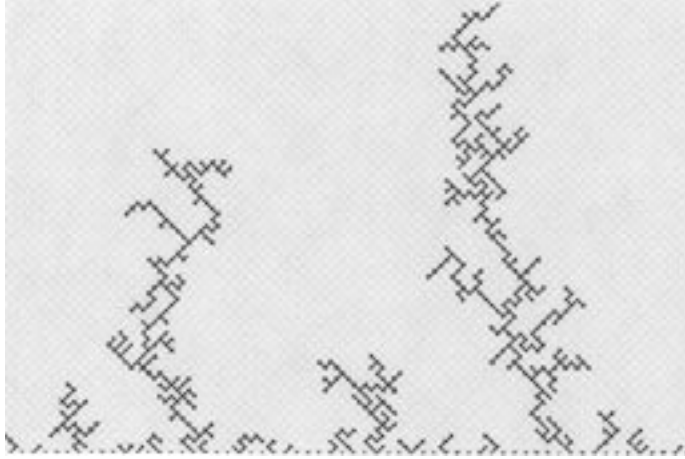


Figure 8. The pattern obtained of a simulation in the regime of viscous fingering on a lattice of 60×80 nodes. $C_a = 4.6 \times 10^{-3}$ and $M = 1.0 \times 10^{-3}$. The invading non-wetting fluid (black) displaces the defending wetting fluid (gray) from below. The simulation took about $7\frac{1}{2}$ h on a Cray T90 vector machine.

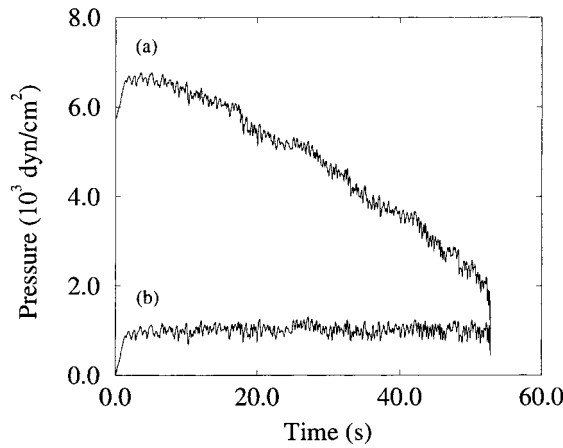


Figure 9. The simulated pressure across the lattice as a function of time (a) and the global capillary pressure (b) for viscous fingering. $C_a = 4.6 \times 10^{-3}$ and $M = 1.0 \times 10^{-3}$. The time is the total time lapse required to let the invading fluid reach the outlet.

the invading fluid at the outlet. The global capillary pressure (b) shows the fluctuations in the capillary pressure when the menisci of the fingertips move through the tubes. We note that the global capillary pressure fluctuates around a mean of 1×10^3 dyn/cm². This is consistent with the average threshold pressure, $\simeq 2\gamma / \langle r_{ij} \rangle$, when r_{ij} is chosen at random in the interval $[0.05, 1.0]$ mm.

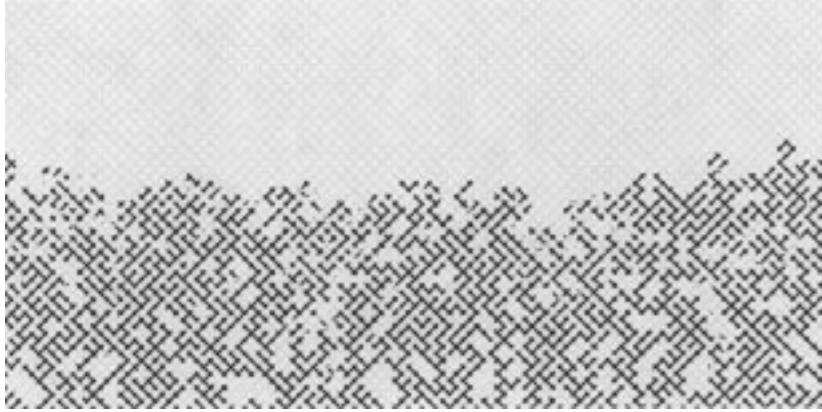


Figure 10. The pattern obtained of a simulation performed on a lattice of 60×60 nodes in the regime of stable displacement. $C_a = 4.6 \times 10^{-3}$ and $M = 1.0 \times 10^2$. The invading non-wetting fluid (black) displacement the defending wetting fluid (gray) from below. The simulation took about 7 hours on a Cray T90 vector machine.

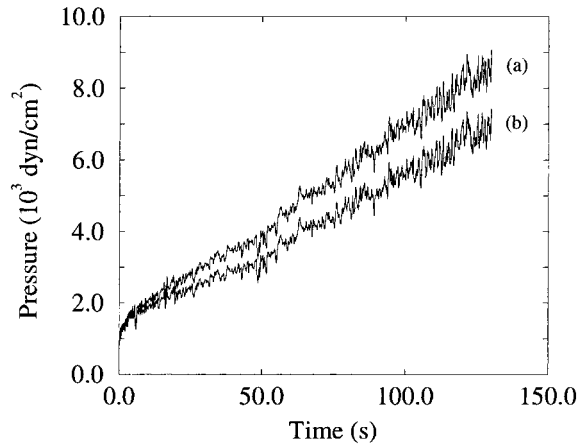


Figure 11. The simulated pressure across the lattice (a) and the global capillary pressure (b) as functions of time for stable displacement. $C_a = 4.6 \times 10^{-3}$ and $M = 1.0 \times 10^2$.

6.2. STABLE DISPLACEMENT

Figure 10 shows the result of a simulation performed in the regime of stable displacement on a lattice of 60×60 nodes. Figure 11 shows the corresponding pressure across the lattice (a) and the global capillary pressure (b) as functions of time. The simulation was stopped when the invading fluid had about half filled the system. The injection rate was $Q = 1.5$ ml/min and the fluid viscosities were $\mu_2 = 10$ P $>$ $\mu_1 = 0.10$ P giving $C_a = 4.6 \times 10^{-3}$ and $M = 1.0 \times 10^2$.

In stable displacement the fluid movements are dominated by the viscous forces in the invading liquid. The viscous pressure gradient in the invading phase is found

to stabilize the front and a compact pattern with an almost flat front between the non-wetting and wetting fluid is generated.

The pressure across the lattice (Figure 11(a)) increases according to the amount of the high viscosity invading fluid injected into the system. The global capillary pressure (b) is also increasing but with a lower rate. The increase is caused by the viscous drag on the trapped clusters of defending fluid left behind the front. At moderate injection rates where the clusters stay in place and keep their shapes the viscous drag is canceled by capillary forces acting on the menisci of the clusters. The sum of those capillary forces contribute to the observed increase in the global capillary pressure.

The fluctuations at the end of the pressure functions seem to increase in amplitude. This is an art effect and is due to small bubbles of non-wetting and wetting fluid that is observed to travel through the network. In the above displacement the viscous forces are strong enough to deform and even move small clusters or bubbles of defending fluid. The moving bubbles increase the number of tubes that should contain three or more menisci. Thus, a large number of reorganizations inside the tubes are applied to avoid more than two menisci in each tube. As mentioned in Section 5.1, this results in unphysical pressure jump causing the pressure function to diverge. For that reason the simulation is stopped before breakthrough of the invading fluid.

6.3. CAPILLARY FINGERING

Figure 12 shows the resulting pattern of a simulation in the regime of capillary fingering and Figure 13 shows the corresponding pressure across the lattice as a

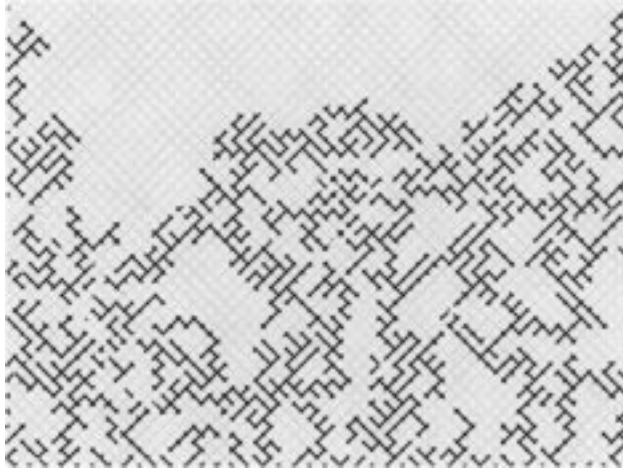


Figure 12. The pattern obtained of a simulation performed on a lattice of 40×60 nodes in the regime of capillary fingering. $C_a = 4.6 \times 10^{-5}$ and $M = 1.0$. The invading non-wetting fluid (black) displacement the defending wetting fluid (gray) from below. The simulation took about 36 h on a Cray T90 vector machine.

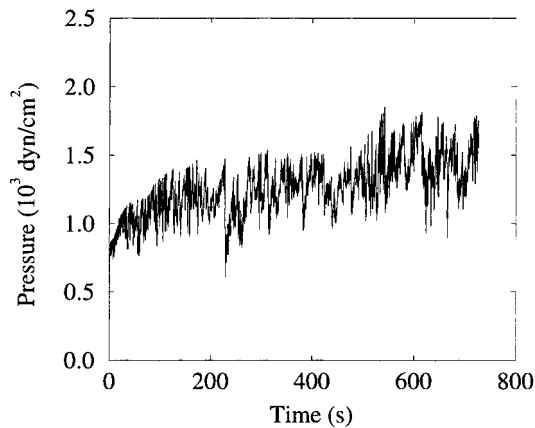


Figure 13. The simulated pressure across the lattice as a function of time for capillary fingering. The fluctuations due to the capillary forces correspond to the burst dynamics of the invading fluid. $C_a = 4.6 \times 10^{-5}$ and $M = 1.0$.

function of time. The simulation was performed on a lattice of 40×60 nodes with injection rate $Q = 0.20$ ml/min. The fluids had equal viscosities, $\mu_1 = \mu_2 = 0.50$ P giving $M = 1.0$ and $C_a = 4.6 \times 10^{-5}$.

In capillary fingering the displacement is so slow that the viscous forces are negligible, with the consequence that the main force is the capillary one between the two fluids. Only the strength of the threshold pressure in the tubes decides if the invading fluid invades that tube or not. Since the radii of the tubes (which determine the threshold pressures) are randomly chosen from a given interval, the non-wetting fluid flows a random path of least resistance.

Figure 12 shows a typical rough front between the invading and the defending fluids with trapped clusters of defending fluid left behind the front. Clusters appear at all sizes between the tube length and the maximum width of the front. The pressure across the lattice (Figure 13) exhibits sudden jumps according to the capillary variation when the non-wetting fluid invades (or retreats) a tube. The jumps are recognized as Haines jumps (Haines, 1930) and the fluctuations identify the bursts where the invading fluid proceeds abruptly (Måløy *et al.*, 1992).

The simulation took 30 h on a Cray T90 vector machine. The reason for this number of hours is the enormous number of time steps required to let the invading fluid reach the outlet. To detect every little burst, tiny step lengths have to be applied. Consequently, in the above simulation approximately 300,000 time steps were required to let the invading fluid reach the outlet, compared to only 2,400 steps in the case of viscous fingering. However, for most simulations the CPU time was about 7–8 h.

Table I. The values for the capillary numbers C_a , injection time, flow rates Q , front width w_s and saturation time t_s for the 17 simulations with $M = 1.0$. The first column lists the number of runs at each capillary number.

Runs	C_a	Injection time (s)	Flow rate (ml/min)	w_s (grid size)	t_s (s)
2	4.6×10^{-5}	731	0.20	11	373
3	9.2×10^{-5}	366	0.40	8.2	187
3	2.3×10^{-4}	153	1.0	7.8	60.0
3	4.6×10^{-4}	78.3	2.0	7.0	33.7
3	9.2×10^{-4}	40.7	4.0	6.9	19.0
3	2.3×10^{-3}	11.0	10	4.6	4.80

6.4. VISCOSITY MATCHING FLUIDS, $M = 1.0$

Table I lists the different capillary numbers, injection times and flow rates for the simulations performed with viscosity matching fluids, $\mu_1 = \mu_2 = 0.50$ P. Also listed are the numbers of simulations done at each capillary number and the front widths and saturation times. Due to limited CPU time we only performed two simulations at $C_a = 4.6 \times 10^{-5}$.

Figure 12 shows an example of a structure obtained from a simulation with low capillary number. The front between the invading (black) and defending (grey) fluid appear as a complicated path connecting the left and right boundary of the lattice. The geometry of the front is analyzed by studying its width and its fractal dimension.

To calculate the front width w we first detected the tubes belonging to the front by running a Hoshen–Kopelman algorithm (Stauffer and Ahrony, 1992) on the lattice. Having found the front tubes we define the width as the standard deviation of the distances between all the front tubes and the average position of the front. Figure 14 shows the front width as functions of time for the different capillary numbers. The functions are calculated by taking the mean of the front width data for the different runs at each capillary number.

The viscous pressure gradient stabilize the front due to trapping of the defending fluid (Frette *et al.*, 1997) and introduces a length scale in the system for large times. In Figure 14 the vertical dashed line indicates the stabilization time t_s where the front width first reaches the saturation width w_s . The saturation width was calculated by taking the mean of the saturation widths for the different runs with same capillary number. The saturation width is indicated by a horizontal dashed line in Figure 14.

We assume that the front width follows the scaling relation (Frette *et al.*, 1997)

$$w \propto t^\beta h\left(\frac{t}{t_s}\right). \quad (23)$$

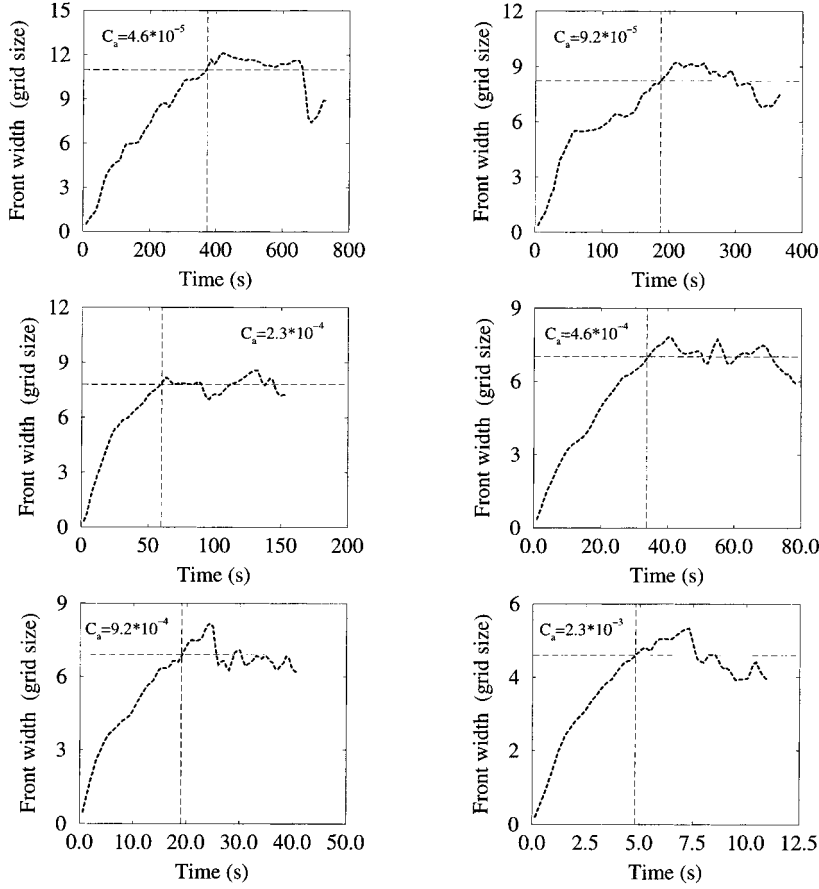


Figure 14. The front width as functions of time for the six capillary numbers. The horizontal dashed line indicate the saturations width w_s and the vertical dashed line indicate the time the front saturates, t_s .

The first term, t^β , describes the time dependence of the front width for small times, that is when $t \ll t_s$. The crossover function $h(t/t_s)$ describes the transition to a stable front. When $t \ll t_s$, $h(t/t_s)$ equals a constant depending on the capillary number only. At large times, $t \gg t_s$, when the front width has saturated the cross over function has the form $h(t/t_s) = (t/t_s)^{-\beta} = t^{-\beta} w_s$.

To find the dynamical exponent β we use the front width data in Figure 14 and plot $\log(w/w_s)$ versus $\log(t/t_s)$. For $t < t_s$ the scaling relation (23) gives $\log(w/w_s) = \beta \log(t/t_s) + c$ where β is the slope and c is a constant. Figure 15 shows the resulting data collapse. The exponent β was estimated to $\beta = 1.0 \pm 0.1$. This is consistent with the experiments by Frette *et al.* (1997) who found $\beta = 0.8 \pm 0.3$.

Both saturation time and saturated front width are functions of the capillary number only. Figure 16 shows t_s (to the left) and w_s (to the right) as functions of C_a . Assuming power law dependences as $t_s \propto C_a^{-\gamma_s}$ and $w_s \propto C_a^{-\alpha}$ we estimate

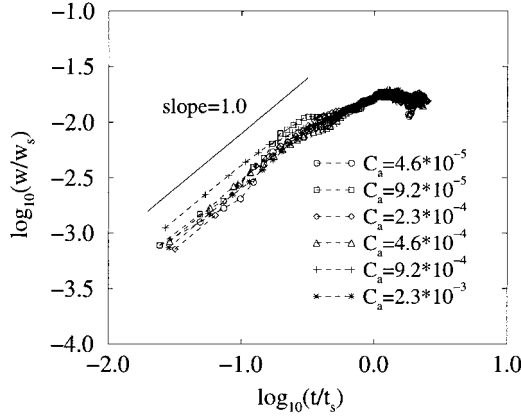


Figure 15. The data collapse for the front width. β is given by the slope then $t/t_s < 1$ and was estimated to $\beta = 1.0 \pm 0.1$.

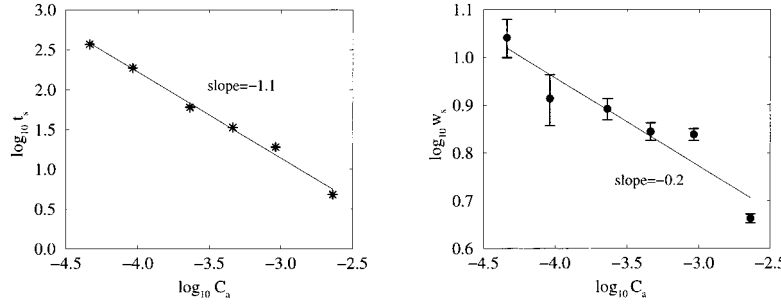


Figure 16. Left: The saturation time t_s as function of capillary number. The solid line has slope -1.1. Right: The saturated front width w_s as function of capillary number. The solid line has slope -0.2. The error bars correspond to the standard error in the mean of the saturation widths.

the exponents to $\gamma_s = 1.1 \pm 0.1$ and $\alpha = 0.2 \pm 0.1$. Unfortunately, the limited size of the lattices and few realizations at each capillary number makes the data poor.

Frette *et al.* (1997) measured the dependence of the saturated front width on the capillary number for viscosity matching fluids. Assuming a power law dependency as $w_s \propto C_a^\alpha$ they concluded that $\alpha = 0.6 \pm 0.2$. Figure 17 shows the saturated front width as function of capillary number for both the result of Frette *et al.* (1997) and our simulations. The saturation width is bounded at maximum by the finite size of the lattice and at minimum by the pore size. Between these boundaries the scaling relation $w_s \propto C_a^{-\alpha}$ is expected to be valid. The limited system size of our simulations makes the difference between minimum and maximum front width small. Consequently, we can only estimate effective values of the scaling exponents α , β and γ_s .

In three dimension Wilkinson proposed the front width to scale with the capillary number as (Wilkinson, 1986) $w_s \propto C_a^{-\nu/(t+1-\beta_o+\nu)}$. Here ν is the correlation length

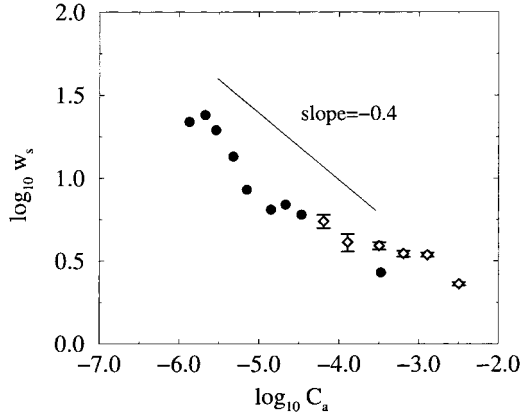


Figure 17. The saturation width w_s as a function of capillary number C_a for both experiments of Frette *et al.* (1997) (filled dots) and simulations (open diamonds). The front widths of the simulations are adjusted due to the pore size of the experiments. The slope of the solid line is -0.4 .

exponent, β_o is the order parameter exponent and t is the conductivity exponent in percolation. If we insert the exponents of two dimensional percolation theory we get $w_s \propto C_a^{-0.38}$. It is hard to extract a scaling exponent of the front width from Figure 17. The solid line has slope -0.4 to indicate the fit of our result with the theory of Wilkinson. We emphasize that his theory is not necessary valid in two dimension due to the trapping of the defending fluid. In three dimensions the trapping can be neglected.

Recently Xu *et al.* (1998) have investigated the scaling behavior of the saturated front width with the capillary number in 2 and 3 dimensions. In 2 dimensions they found from numerical pore-network simulations that $w_s \propto C_a^{-0.34}$.

The fractal structure of the front is characterized by using the box counting method. In the box counting procedure, the number of boxes $N(l)$ required to cover the front scales with the box size l as

$$N(l) = N_0 w^{-D_b} f\left(\frac{l}{w}\right). \quad (24)$$

Here N_0 is the number of front tubes. The crossover function $f(l/w)$ describes the transition between the upper and the lower cut off lengths in the system. In our case the cut off lengths corresponds to the tube length $l = 1$, and the front width $l = w$, respectively. Between the cut off lengths we expect a data collapse when $\log(N(l)w^{D_b}/N_0)$ is plotted against $\log(l/w)$ for the box counting data. The data collapse is shown in Figure 18 and from the slope we estimated the fractal dimension to $D_b = 1.3 \pm 0.2$. The result is consistent with experiments performed by Frette *et al.* (1997) and close to the fractal dimension of external perimeter of percolation clusters, $D_e = 4/3$ (Grossmann and Aharony, 1986a; Grossmann and Aharony, 1986b).

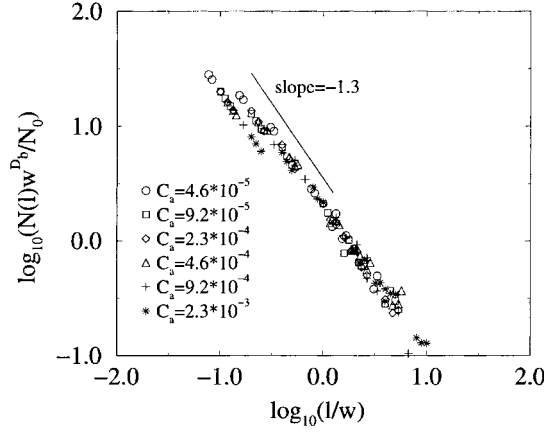


Figure 18. The data collapse from the box counting data of the front width w for the 17 simulations. The fractal dimension was found from the slope of the plot to be $D_b = 1.3 \pm 0.2$.

7. Conclusions

We have presented and discussed a two-dimensional network model simulating the time dependencies of different properties in drainage displacement. In particular we have focused on the temporal evolution of the pressure across the lattice and the global capillary pressure as defined in Equation (9). Moreover, we have studied the time dependence of the front width on the capillary number. We found the front to have fractal dimension $D_b = 1.3$ and the width to follow the scaling relation $w \propto t^\beta h(t/t_s)$. The dynamics exponent β was estimated to $\beta = 1.0 \pm 0.1$. The results are in good quantity agreement with experimental data of Frette *et al.* (1997).

An important feature of the model is the capability to study temporal evolutions of the pressure across the system and the global capillary pressure. This is a great advance since corresponding measurements in experimental setups are too difficult. A quantification of the pressure behavior will be addressed in future work. With the proposed model it is also possible quantify the competition between viscous and capillary forces in the displacement. This will help to characterize the different flow regimes observed in drainage.

The model simulates the dynamics of drainage dominated flow where film flow can be neglected. The local capillary pressure of the moving menisci is a continuous function depending on the tube's effective radii as if they were hour-glass shaped. The numerical solution due to this dynamic costs computation time, but it is valuable for getting a more complete knowledge of the displacement process.

An approximation has been developed to simulate simultaneous flow of the two liquids into one tube. The presented moving rules take care of this sort of mixing and actually, they are essential to make the model work. So far the moving rules are based on the mechanisms observed in drainage, but in principle it should be possible by a certain modifications to model imbibition as well.

The lattice sizes are limited by the computation time and the model requires usage of high performance vector machines. To afford simulations on lattice sizes comparable to those in experimental setups (Måløy *et al.*, 1985; Frette *et al.*, 1997), more sophisticated and efficient algorithms have to be developed, for example though the use of various acceleration schemes such as Fourier Acceleration (Batrouni and Hansen, 1988). Furthermore, vector machines with parallel capabilities should be considered.

Acknowledgements

We thank S. Basak, I. O. Frette and J. Schmittbuhl for valuable comments. The computations were done at HLRZ, Forschungszentrum Jülich GmbH and E.A. is grateful for the hospitality shown there. The work has received support from NFR, The Research Council of Norway.

References

- Batrouni, G. G. and Hansen, A.: 1988, Fourier acceleration of iterative processes in disordered systems, *J. Stat. Phys.* **52**, 747–773.
- Blunt, M. and King, P.: 1990, Macroscopic parameters from simulations of pore scale flow, *Phys. Rev. A* **42**, 4780–4787.
- Cieplak, M. and Robbins, M. O.: 1988, Dynamical transition in quasi-static fluid invasion in porous media, *Phys. Rev. Lett.* **60**, 2042–2045.
- Chen, J.-D. and Wilkinson, D.: 1985, Pore-scale viscous fingering in porous media, *Phys. Rev. Lett.* **55**, 1892–1895.
- Constantinides, G. N. and Payatakes, A. C.: 1996, Network simulation of steady-state two-phase flow in consolidated porous media, *AIChEJ* **42**, 369–382.
- Dias, M. M. and Payatakes, A. C.: 1986, Network models for two-phase flow in porous media. Part 1. Immiscible micro-displacement of non-wetting fluids, *J. Fluid Mech.* **164**, 305–336.
- Dullien, F. A. L.: 1992, *Porous Media: Fluid Transport and Pore Structure*, Academic Press, San Diego, pp. 333–336.
- Dussen, V. E. B.: 1979, On the spreading of liquids on solid surfaces: static and dynamic contact lines, *Ann. Rev. Fluid Mech.* **11**, 371–400.
- Frette, O. I., Måløy, K. J., Schmittbuhl, J. and Hansen, A.: 1997, Immiscible displacement of viscosity matched fluids in two-dimensional porous media, *Phys. Rev. E* **55**, 2969–2975.
- Haines, W. B.: 1930, Studies in the physical properties of soil, *J. Agr. Sci.* **20**, 97–116.
- Grossmann, T. and Aharony, A.: 1986a, Structure and perimeters of percolation clusters, *J. Phys. A* **19**, L745–L751.
- Grossmann, T. and Aharony, A.: 1986b, Accessible external perimeters of percolation clusters, *J. Phys. A* **20**, L1193–L1201.
- King, P. R.: 1987, The fractal nature of viscous fingering in porous media, *J. Phys. A* **20**, L529–L534.
- Koplik, J. and Lasseter, T. J.: 1985, Two-phase flow in random network models of porous media, *SPE J.* **2**, 89–100.
- Lenormand, R., Touboul, E. and Zarcone, C.: 1988, Numerical models and experiments on immiscible displacements in porous media, *J. Fluid Mech.* **189**, 165–187.
- Lenormand, R. and Zarcone, C.: 1983, Mechanism of the displacement of one fluid by another in a network of capillary ducts, *J. Fluid Mech.* **135**, 337–353.

- Lenormand, R. and Zarcone, C.: 1985, Invasion percolation in an etched network: measurement of a fractal dimension, *Phys. Rev. Lett.* **54**, 2226–2229.
- Måløy, K. J., Feder, J. and Jøssang, T.: 1985, Viscous fingering fractals in porous media, *Phys. Rev. Lett.* **55**, 2688–2691.
- Måløy, K. J., Furuberg, L., Feder, J. and Jøssang, T.: 1992, Dynamics of slow drainage in porous media, *Phys. Rev. Lett.* **68**, 2161–2164.
- Paterson, L.: 1984, Diffusion-limited aggregation and two-fluid displacements in porous media, *Phys. Rev. Lett.* **52**, 1621–1624.
- Pereira, G. G., Pinczewski, W. V., Chan, D. Y. C., Paterson, L. and Øren, P. E.: 1996, Pore-scale network model for drainage-dominated three-phase flow in porous media, *Transport in Porous Media* **24**, 167–201.
- Press, W. H., Teukolsky, S. A., Vetterling, W. T. and Flannery, B. P.: 1992, *Numerical Recipes*, Cambridge University Press, New York, NY, pp. 704–708.
- Stauffer, D. and Aharony, A.: 1992, *Introduction to Percolation Theory*, Taylor & Francis, London, Great Britain.
- van der Marck, S. C., Matsuura, T. and Glas, J.: 1997, Viscous and capillary pressures during drainage: Network simulations and experiments, *Phys. Rev. E* **56**, 5675–5687.
- Xu, B., Yortsos, Y. C. and Salin, D.: 1998, Invasion percolation with viscous forces, *Phys. Rev. E* **57**, 739–751.
- Washburn, E. W.: 1921, The dynamics of capillary flow, *Phys. Rev.* **17**, 273–283.
- Wilkinson, D.: 1986, Percolation effects in immiscible displacement, *Phys. Rev. A* **34**, 1380–1391.
- Wilkinson, D. and Willemsen, J. F.: 1983, Invasion percolation: A new form of percolation theory, *J. Phys. A* **16**, 3365–3376.
- Witten, T. A. and Sander, L. M.: 1981, Diffusion-limited aggregation, a kinetic critical phenomenon, *Phys. Rev. Lett.* **47**, 1400–1403.